

Exceptional Thermoelectric Properties of Layered GeAs₂

Fancy Qian Wang,[†] Yaguang Guo,[†] Qian Wang,^{*,†,‡} Yoshiyuki Kawazoe,^{‡,§} and Puru Jena^{||}

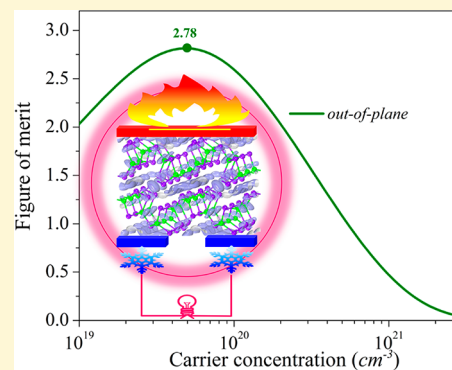
[†]Center for Applied Physics and Technology, College of Engineering, Peking University, Key Laboratory of High Energy Density Physics Simulation, Ministry of Education, Beijing 100871, China

[‡]New Industry Creation Hatchery Center, Tohoku University, Sendai 980-8577, Japan

[§]Department of Physics and Nanotechnology, Sri Ramaswamy Memorial University, Kattankulathur 603203, TN, India

^{||}Department of Physics, Virginia Commonwealth University, Richmond, Virginia 23284, United States

ABSTRACT: Using semiclassical Boltzmann transport theory and density functional formalism, we have systematically studied the thermoelectric performance of layered GeAs₂. The figure of merit, ZT value, of this layered structure is found to be 2.78 along the out-of-plane direction, with optimal carrier concentration at 800 K. Analysis of the charge density difference and phonon transport properties allows us to attribute such exceptional thermoelectric properties to strong interlayer interaction between the adjacent layers where quasicovalent bonding is responsible for the enhanced electrical conductivity, while the layered structure accounts for the suppressed lattice thermal conductivity. This study highlights the potential of layered crystals for highly efficient thermoelectric materials.



INTRODUCTION

Layered materials have attracted considerable attention due to their unique properties.^{1–3} In specific cases, the ability to extract individual layers has also made it possible to explore the effect of nanostructures on their electronic,^{4–6} magnetic, and optical properties.⁷ The interlayer coupling can either be weak van der Waals (vdW) such as in graphite or sizable quasicovalent bonding such as in black phosphorus,^{8–11} PtS₂,¹² and PtSe₂.¹³ The latter exhibits strong layer-dependent electronic^{8,12} and vibrational properties.^{11,12} For example, platinum disulfide (PtS₂) has been reported to possess a nearly isotropic in-plane and out-of-plane mechanical interlayer coupling due to quasicovalent bonding formed by strong orbital hybridization of interlayer sulfur atoms.¹² Similarly, the well-known direct to indirect band gap transition in MoS₂ arises from the Coulomb repulsion between the sulfur atoms in adjacent layers.^{14,15} These results imply that strong quasicovalent bonding, rather than pure vdW force, is primarily responsible for some of the distinctive electronic^{16–18} and mechanical properties^{19,20} of these materials.

On the other hand, the interface between adjacent layers in layered structures generates a large phonon anharmonicity, leading to dissipative phonon transport and ultralow intrinsic lattice thermal conductivity between the adjacent layers. Such characteristics enable layered materials to have great potential as highly efficient thermoelectric materials. Unfortunately, due to the absence of effective bonding in conventional vdW layered materials, the electrical conductivity σ is usually low between the adjacent layers. Thus, if we can find some special layered material with strong interlayer coupling such as

quasicovalent bonding, then it may be possible to achieve a high ZT value in such materials.

In this work, we focus on such a layered material, germanium diarsenide (GeAs₂). Because of its small vertical interlayer spacing (~ 1 Å), the interlayer interactions are not vdW-like and, thus, are not negligible. As a result, we expect that GeAs₂ may exhibit some novel transport properties. We note that GeAs₂ was recently predicted to be a promising candidate material for both n- and p-type thermoelectric systems, based upon a semiempirical descriptor β_{SE} .²¹ However, the optimal ZT values and the details of the direction-dependent transport properties are still not understood. Here, we systematically study the thermoelectric properties of GeAs₂ including its Seebeck coefficient, electrical conductivity, thermal conductivity, and figure of merit, ZT. We find the optimal ZT value to be 2.78 along the out-of-plane direction, with the electron doping concentration of $\sim 3 \times 10^{20}$ cm⁻³ at 800 K. This result demonstrates that strong interlayer interactions play an important role in thermoelectric properties.

COMPUTATIONAL METHODS

Our first-principles calculations are carried out using density functional theory (DFT) and generalized gradient approximation (GGA) for exchange–correlation potential as given by Perdew–Burke–Ernzerhof (PBE).²² The projector augmented wave (PAW) method implemented in the Vienna *ab initio* simulation package (VASP)²³ is used with an energy cutoff of 400 eV for the plane-wave basis. The Monkhorst–Pack k-point mesh of $5 \times 4 \times 14$ is used to sample the

Received: August 3, 2017

Revised: October 8, 2017

Published: October 8, 2017

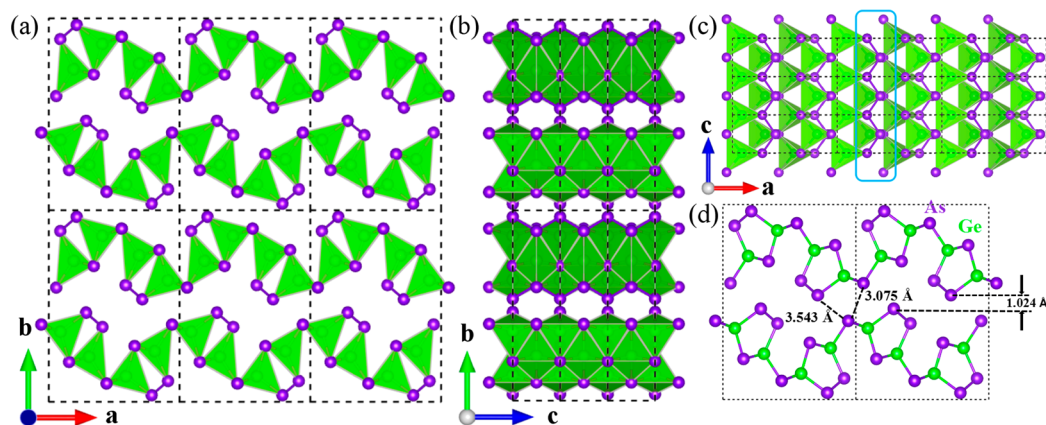


Figure 1. (a) Front, (b) side, and (c) top views of the fully optimized geometry of GeAs₂ crystal in a 3 × 2 × 3 supercell. (d) Optimized GeAs₂ structure with the As–As atomic distances and the interlayer spacing. The green tetrahedra and black dashed rectangles correspond to the building blocks and the primitive cells of bulk GeAs₂, respectively.

irreducible Brillouin zone. The energy convergence threshold is set to 10^{−6} eV. In optimizing the structure, van der Waals interactions are taken into account using the semiempirical correction of Grimme.^{24,25} Both the cell shape and volume are fully optimized, and all of the atoms are allowed to relax until the maximal Hellmann–Feynman force acting on each atom is less than 0.01 eV/Å.

To calculate the electrical conductivity σ and the Seebeck coefficient S , the Boltzmann transport equation (BTE) is solved, combined with the single parabolic band (SPB) model^{26,27} for the relaxation time τ . Since an accurate description of band gap is critical to predict the performance of thermoelectric materials, the electronic band structure is calculated using the Tran–Blaha modified Becke–Johnson (TB-mBJ) exchange potential,^{24,28} which is especially designed for obtaining a band gap closer to the experimental result and has been widely applied to other systems.^{29–31} The energy-dependent electrical conductivity σ and Seebeck coefficient S are calculated as

$$\sigma = \frac{e^2}{\Omega} \int \tau(\vec{k}) v(\vec{k}) v(\vec{k}) \left[-\frac{\partial f^0(\epsilon_k)}{\epsilon_k} \right] d\epsilon \quad (1)$$

$$S = \frac{e}{\sigma T} \int \tau(\vec{k}) v(\vec{k}) v(\vec{k}) (\epsilon_k - \epsilon_f) \left[-\frac{\partial f^0(\epsilon_k)}{\epsilon_k} \right] d\epsilon \quad (2)$$

where Ω is the volume of the unit cell, $\tau(\vec{k})$ represents relaxation time, $v(\vec{k}) = \frac{1}{\hbar} \nabla_{\vec{k}} \epsilon_{\vec{k}}$ is the group velocity, ϵ_f is the Fermi energy, and f^0 is the Fermi–Dirac distribution function. The lattice thermal conductivity κ_{lat} is calculated by exactly solving the linearized phonon BTE combined with an iterative approach to determine phonon relaxation time.^{32,33} The microscopic description of κ_{lat} along the α -direction is given as the sum of contributions over all the phonon modes $\lambda(\mathbf{q}, j)$ with the wave vector \mathbf{q} and branch index j , namely, $\kappa_{\alpha} = \frac{1}{N_q V} \sum_{\lambda(\vec{q}, j)} C_{\lambda(\vec{q}, j)} v_{\lambda(\vec{q}, j)\alpha}^2 \tau_{\lambda(\vec{q}, j)}$. Here, $C_{\lambda(\vec{q}, j)}$, $v_{\lambda(\vec{q}, j)\alpha}$, and $\tau_{\lambda(\vec{q}, j)}$ are, respectively, the specific heat contribution, phonon group velocity, and phonon relaxation time of every phonon mode $\lambda(\mathbf{q}, j)$. N_q is the number of sampled \mathbf{q} points in the Brillouin zone, and V is the volume of the unit cell. The harmonic and anharmonic interatomic force constants are obtained using 3 × 1 × 4 and 2 × 2 × 4 supercells as inputs to the phonon BTE for calculating κ_{lat} . The cutoff radius of 4 Å is chosen to ensure accuracy of our calculations. The translation invariance conditions are imposed on the force constants. The electronic thermal conductivity κ_e is calculated using the Wiedemann–Franz law, $\kappa_e = L\sigma T$, where L is the Lorenz constant, and is set to 1.5 × 10^{−8} W Ω K^{−2}, which is adequate for some semiconductors.^{34,35}

RESULTS AND DISCUSSION

Structure Optimization. Bulk GeAs₂ possesses *Pbam* symmetry (D_{2h}^9 , 55) and adopts a layered orthorhombic crystal structure consisting of 8 Ge and 16 As atoms in the primitive unit cell. The crystal structure of GeAs₂, given in Figure 1, shows that the GeAs₂ layers are stacked against each other along the b -axis. The optimized lattice constants are $a = 10.153$ Å, $b = 14.841$ Å, and $c = 3.707$ Å, respectively, and are in good agreement with experimental results.^{36,37} The building block of GeAs₂, marked with green tetrahedra, is composed of one Ge atom tetrahedrally bonded to its nearest four As atoms. Two adjacent tetrahedra are bonded together, forming the quasi-one-dimensional structure via the zigzag As–As covalent chains (marked with a blue solid box) along the c -axis in Figure 1c. Meanwhile, they are connected with each other through As–Ge covalent bonds after rotating about the a -axis. In addition, we note that each layer is terminated by As atoms with the shortest As–As distance of 3.08 Å. The vertical interlayer spacing is 1.02 Å, as shown in Figure 1d, which is much smaller than that in many other layered materials such as bulk black phosphorus (3.27 Å)²⁰ and platinum disulfide (2.54 Å).¹²

Energy Band Structure. Figure 2 shows the electronic band structure of GeAs₂, which is semiconducting with an indirect band gap of 0.96 eV calculated at the TB-mBJ level. This is close to the experimental optical gap (~1.06 eV).³⁸ Two distinctive features can be observed: The edges of the valence bands yield several hole pockets, labeled as VBM, VB2, VB3, and VB4; they are nearly energetically degenerate with an energy difference less than 0.16 eV. This is similar to that of other well-known thermoelectric materials such as PbTe (0.15 eV)³⁹ and SnSe (0.15 eV).^{40–42} These hole pockets with large density of states (DOS) were found to lead to an enhanced Seebeck coefficient.⁴² Meanwhile, the edges of conduction bands (CBs), labeled as CBM and CB2, exhibit a “pudding-mold-like” shape, which has been found to be favorable for thermoelectric performance.^{43,44}

Electronic Transport Coefficients. We next study the Seebeck coefficient (S) of GeAs₂. Since the melting point of bulk GeAs₂ is about 1000 K,³⁸ we choose 300 and 800 K as typical temperatures for thermoelectric calculations. Figure 3a shows the calculated S as a function of carrier concentration for p- and n-type GeAs₂ at 300 and 800 K, respectively. The Seebeck coefficient S decreases significantly with increasing carrier concentration for both p- and n-type GeAs₂ due to the

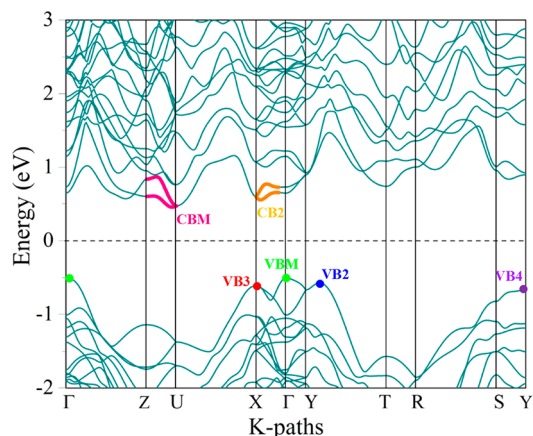


Figure 2. Calculated band structure of bulk GeAs₂ crystal using the TB-mBJ functional. Several hole (electron) pockets are marked by different color points (lines). The VB(M) and CB(M) stand for the valence band (maximum) and conduction band (minimum), respectively.

bipolar conduction effect.³ The S of p-type GeAs₂ exhibits anisotropy at 300 K ($S_b > S_c > S_a$), and the largest value of $\sim 400 \mu\text{V/K}$ appears along the b -axis because of the large density of states effective mass m_{dos}^* . However, S_b decreases significantly with increasing hole concentration, and then becomes smaller than S_a and S_c when hole concentration is larger than $1 \times 10^{21} \text{ cm}^{-3}$, indicating that other heavy bands might contribute to carrier transport along the in-plane rather than the out-of-plane direction.⁴⁵ Similar behavior is also observed at 800 K in p-type GeAs₂. In contrast, at 300 K, the S of n-type GeAs₂ is insensitive to the directions in the region of

low carrier concentration, and is quite small as compared to that of its p-type counterpart, especially for electron concentrations below $4 \times 10^{20} \text{ cm}^{-3}$ due to the smaller m_{dos}^* . When temperature increases to 800 K, S_c becomes larger than S_a and S_b , respectively, in the whole range of carrier concentration and reaches the largest value of $550 \mu\text{V/K}$ at electron concentration of $5.4 \times 10^{18} \text{ cm}^{-3}$. A different trend of S for the p- and n-type GeAs₂ crystals results from different shapes of their band edges. A similar behavior is also observed in SnSe.⁴⁶

To calculate the electrical conductivity σ , relaxation time τ is required as the output value in BoltzTraP code⁴⁷ is σ/τ . However, determining τ is difficult because it depends on both temperature and carrier concentration. An approximate constant relaxation time of 10 fs, which has been used in some recent studies,^{44,48–51} causes severe limitations in quantifying their ZT value. In our present study, the single parabolic band model (SPB) is used to obtain reliable τ , which has been successfully applied to predict ZT values in many thermoelectric materials.^{42,52–54} We calculate the energy-dependent relaxation time $\tau(E)$ by using $\tau(E) = \tau_0 E^s$, where s is related to specific scattering mechanism, and is set as $-1/2$, because the predominant scattering in the low energy region mainly comes from the coupling between the free carriers and the acoustic phonons. In addition, according to Bardeen and Shockley's theory,⁵⁵ the acoustic phonon scattering in the long wavelength limit is modeled by the deformation potential (DP), in which the scattering matrix element takes the form $M(\vec{k}, \vec{k}')^2 = \frac{k_B T E_1^2}{C_{ii}}$, where C_{ii} and E_1 are the elastic constant and the deformation potential constant, respectively.^{56,57} Thus,

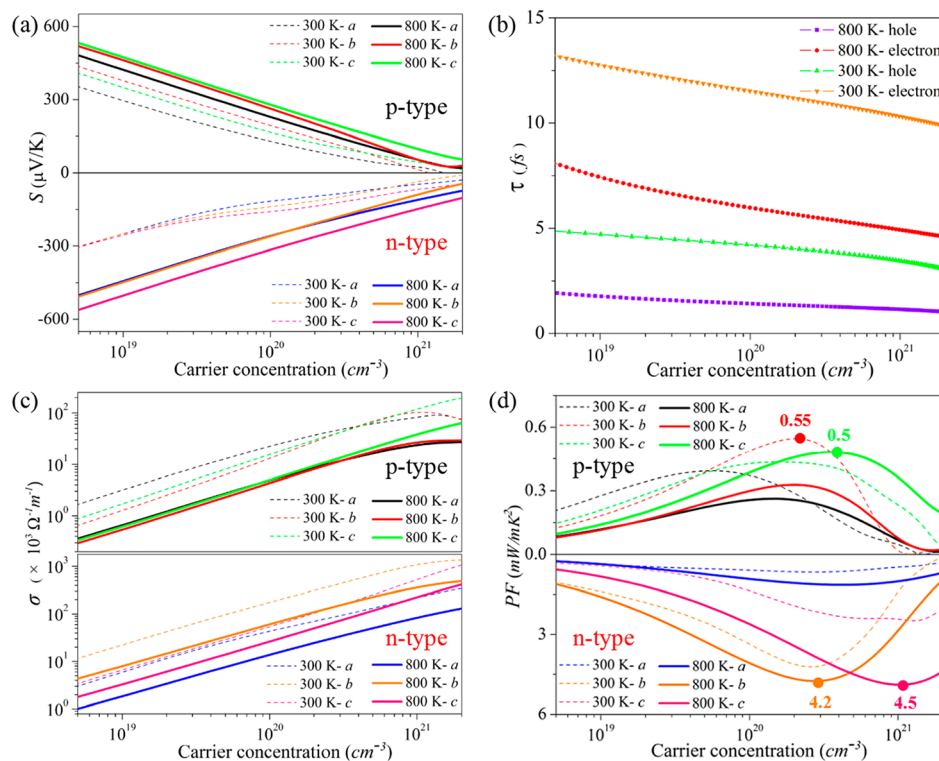
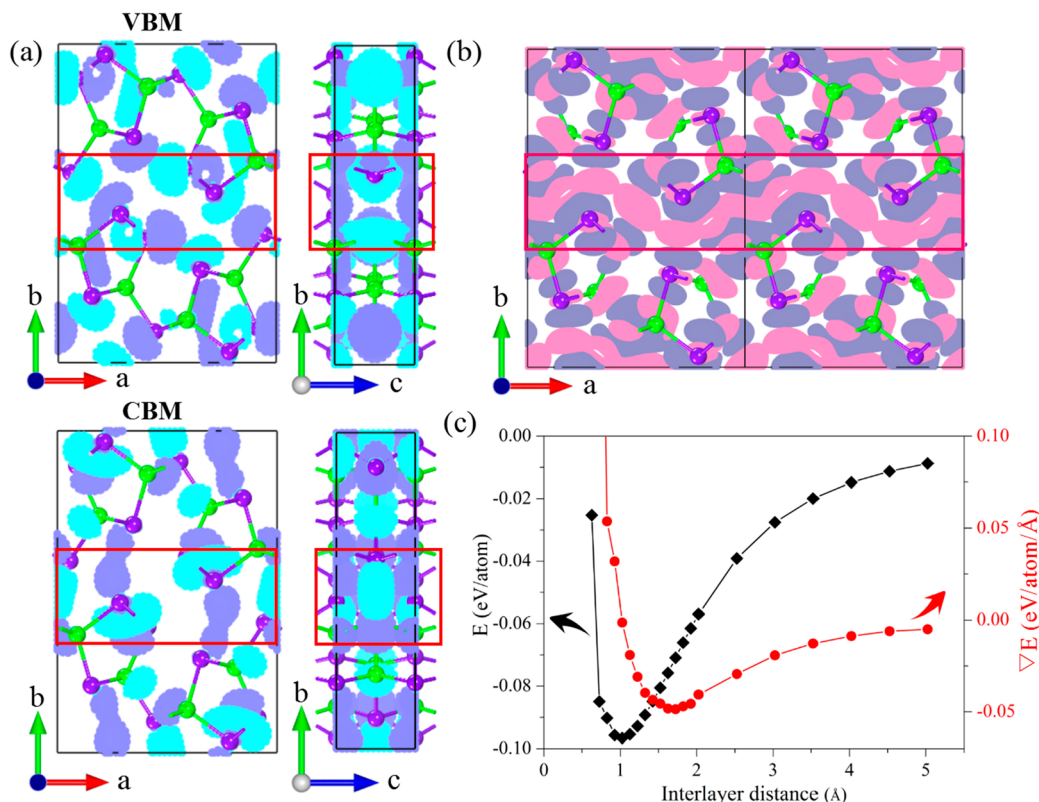


Figure 3. Calculated electronic transport properties of p-type and n-type GeAs₂ as a function of carrier concentration along three axes at 300 K (---) and 800 K (—): (a) Seebeck coefficient S , (b) average relaxation time τ as a function of temperature and carrier concentration for both electrons and holes, (c) electrical conductivity σ , and (d) power factor (PF).

Table 1. Effective Mass m^* , Elastic Constant C_{ij} and Deformation Potential Constant E_1 Obtained from First-Principles Calculations Used for the SPB Model

carrier	m^* (m_e)			E_1 (eV)			C_{ij} (Gpa)		
	a	b	c	a	b	c	a	b	c
hole (h)	0.20	0.84	0.44	13.62	9.35	8.80	23.06	55.22	100.64
electron (e)	0.34	0.15	0.46	6.85	9.93	7.62	23.06	55.22	100.64

**Figure 4.** Spatial distribution of wave functions for the (a) VBM and CBM illustrated in the ab -planes using an isosurface of 0.025 e Å. (b) Calculated charge density difference, where the regions of electron excess and electron deficiency are marked by gray and pink, respectively, and the interlayer regions are marked by the red rectangles. (c) Calculated binding energy E and its derivatives ∇E of bilayer GeAs_2 as a function of the interlayer distance. The value of the first red dot (out-of-range) is 0.60 eV/atom/Å.

the acoustic phonon scattering-limited relaxation time τ_0 is given by

$$\tau_0 = \frac{h^4 C_{ii}}{8\pi^3 k_B T (2m^*)^{3/2} E_1^2} \quad (3)$$

where h is the Planck constant and m^* is the single valley density of states effective mass.⁵⁴ The calculated m^* , C_{ij} , and E_1 are given in Table 1. The variation of τ with carrier concentration at 300 and 800 K is plotted in Figure 3b. We note that τ varies over a large range from 2 to 13 fs. This behavior seems reasonable because the scattering of carriers occurs more frequently at higher temperatures and carrier concentrations, as is the case with layered GeSe.⁴⁵ In addition, the electron relaxation time is more than 2 times larger than the hole relaxation time, due to the smaller effective mass and deformation potential constant.

Inserting the relaxation time to σ/τ , we obtain σ as a function of carrier concentration at 300 and 800 K. The results are given in Figure 3c. Anisotropic σ is observed for p-type GeAs_2 at 300 K, as a result of different hole effective masses along the a , b , and c axes. However, this anisotropy is not obvious at 800 K in the region of low hole concentration (lower than 5×10^{20}

cm^{-3}). For n-type GeAs_2 , σ shows larger magnitudes than that of its p-type counterpart due to the much larger τ . An interesting feature occurs in n-type GeAs_2 : σ_b , namely, the out-of-plane electrical conductivity, is even larger than the in-plane values (σ_a and σ_c) at both 300 and 800 K.

To ascertain the strength and nature of the interlayer interaction in GeAs_2 , we first calculate the wave functions for the VBM and CBM to visualize the orbital overlap between the atoms. These are shown in Figure 4a. Interestingly, a reversed bonding feature is observed; namely, the VBM and CBM exhibit antibonding and bonding states, respectively, indicating the existence of strong electronic hybridization of the lone pair electrons of the terminal As atoms between the adjacent layers.¹²

Next, we calculate the charge density difference, and observe a significant charge redistribution in GeAs_2 . The electron deficiency between the adjacent layers of GeAs_2 confirms its covalent bonding character of the interlayer interaction (see Figure 4b). The calculated binding energy and its derivatives of bilayer GeAs_2 , shown in Figure 4c, are quite large compared to that of graphene¹⁰ and bilayer MoS_2 .¹⁰ Moreover, the binding energy of GeAs_2 (~ 0.1 eV/atom) at its equilibrium state is

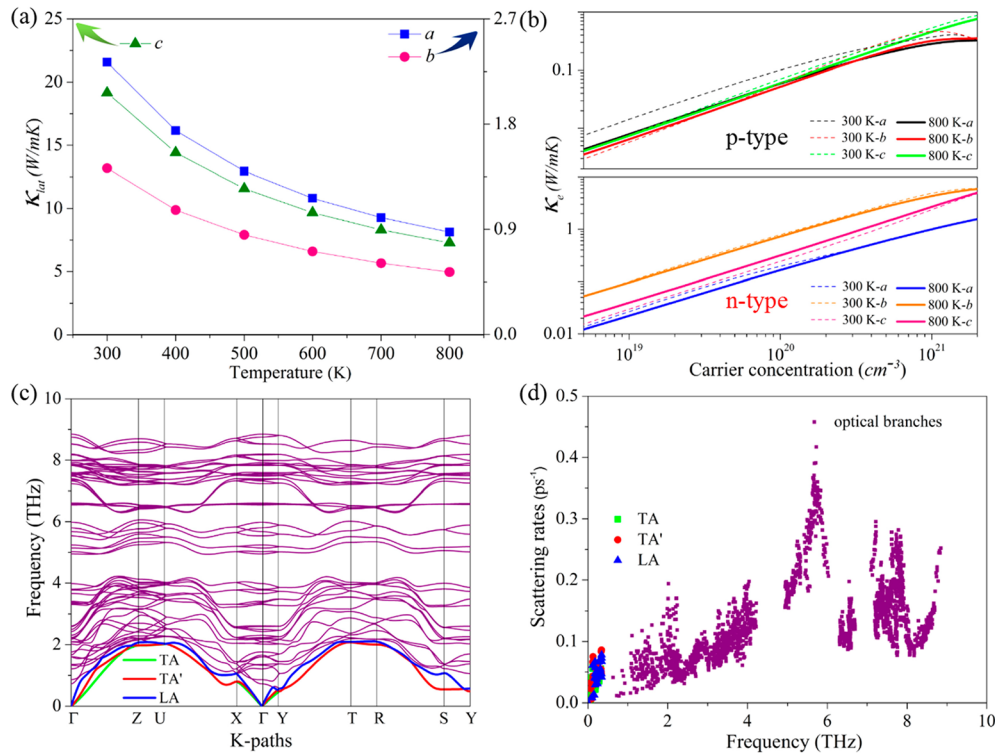


Figure 5. (a) Calculated lattice thermal conductivity κ_{lat} and (b) electronic thermal conductivity κ_e along the three axes. (c) Calculated phonon dispersion and (d) variation of three-phonon scattering rates of each scattering mode with the frequency of GeAs_2 .

much larger than that of black phosphorus (~ 0.08 eV/atom)⁹ and PtS_2 (0.05 eV/atom),⁵⁸ which are found to possess a strong interlayer interaction. In addition, the vertical interlayer spacing of GeAs_2 (1.02 Å) is much smaller than those of PtS_2 (2.54 Å) and black phosphorus (3.27 Å). All of these features imply that the interlayer interaction of GeAs_2 is associated with the quasicovalent bonding, rather than pure vdW forces, thus providing channels for electron transport, which gives reasonable explanation for the large σ_b .

Considering that S (σ) decreases (increases) with carrier concentration, we further calculate the power factor ($S^2\sigma$), which represents the coupling effects between S and σ , for optimizing thermoelectric performance. The results are displayed in Figure 3d. The power factor initially increases and then decreases with increasing carrier concentration since doping generally favors σ over S . It exhibits similar dependence on carrier concentration and direction for both p-type and n-type GeAs_2 at different temperatures. However, n-type GeAs_2 possesses a significantly larger power factor than its p-type counterpart because of the relatively large electrical conductivity. The highest value of p-type GeAs_2 is 0.55 (0.50) mW/mK^2 along the b (c)-direction at 300 (800) K with the concentration of $\sim 1 \times 10^{20}$ (3×10^{20}) cm^{-3} . On the other hand, for n-type GeAs_2 , the optimal power factor of 4.5 mW/mK^2 along the c -axis with electron concentration of $\sim 1 \times 10^{21}$ cm^{-3} arises from the strong zigzag As–As covalent chains. Similarly, power factors of ~ 4.2 mW/mK^2 arise with a lower carrier concentration $\sim 2 \times 10^{20}$ cm^{-3} along the b -direction. Such high values of the power factors are comparable to those of typical thermoelectric materials, such as SnSe (~ 4 mW/mK^2)⁴¹ and PbTe (~ 2.5 mW/mK^2).⁵⁹

Thermal Transport Coefficients. As mentioned above, thermal conductivity is also crucial to the ZT value. Thus, we calculate both the lattice conductivity, κ_{lat} , and electronic

conductivity, κ_e . As shown in Figure 5a, a low out-of-plane κ_b of 1.42 (0.53) W/mK is obtained at 300 K (800 K), due to strong anharmonicity between the interlayers. Meanwhile, the in-plane κ_{lat} , κ_a , and κ_c are calculated to be 2.33 (0.87) and 19.16 (7.28) W/mK at 300 K (800 K), respectively, leading to a much larger anisotropy ratio (κ_c/κ_a) of 6.55 (8.37) as compared to that of other anisotropy crystals such as SnSe (~ 1)⁴⁸ and phosphorene (3.44).⁶⁰ To understand this large anisotropy, we calculate the phonon dispersion, which contains detailed information on the vibrational states.⁶¹ The results are shown in Figure 5c, where the two transverse acoustic phonon scattering branches (TA and TA') are plotted in green and red lines, respectively; the longitudinal acoustic phonon modes (LA) are plotted in blue lines, and all other optical branches are plotted in purple. On the basis of the phonon dispersion, the phonon velocity V_g and the longitudinal Debye temperature Θ are evaluated and given in Table 2. Although the V_g values of three acoustic branches

Table 2. Calculated Phonon Velocity V_g and Longitudinal Debye Temperature Θ for Three Acoustic Branches

direction	V_g (km/s)			Θ (K)		
	TA	TA'	LA	TA	TA'	LA
Γ –X (a -axis)	14.28	19.93	17.48	38.21	38.22	51.04
Γ –Y (b -axis)	16.58	22.55	20.02	22.82	24.84	29.31
Γ –Z (c -axis)	48.64	23.11	31.94	94.82	95.02	99.82

are similar along the Γ –X (a -axis) and Γ –Y (b -axis) directions, the TA and LA modes exhibit much larger V_g along the Γ –Z (c -axis) direction than that along the other two directions. Besides, the Θ_c is significantly larger than the Θ_a and Θ_b . These two features indicate that κ_c is much larger than κ_a and κ_b . In addition, the optical branches are relatively localized along the Γ –X and Γ –Y directions, while they are much more dispersive

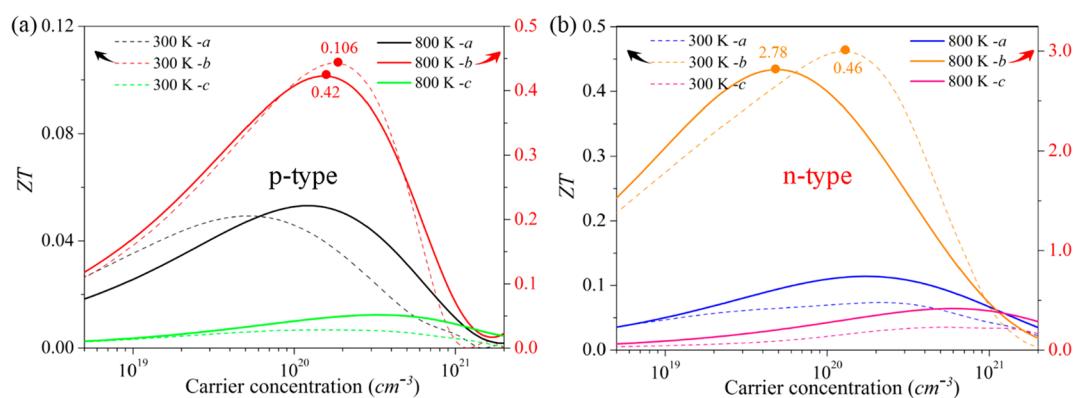


Figure 6. Calculated figure of merit ZT along the three axes for (a) p-type and (b) n-type GeAs_2 as a function of carrier concentration at 300 and 800 K.

and even comparable to those of acoustic branches along the Γ -Z direction, especially below 4 THz. Thus, V_g of the optical branches along the Γ -Z direction is larger than that along the other two directions, resulting in a large anisotropy of κ_{lat} . Meanwhile, the low frequency optical branches also make a considerable contribution to κ_{lat} because of their large V_g .

To verify the above analysis, we further calculate the frequency-dependent three-phonon scattering rates. The results are shown in Figure 5d. In accordance with the phonon gap, a remarkable scattering gap is observed between 4 and 6 THz. Note that the scattering rates of the acoustic branches and optical branches are comparable, especially at low frequency. Thus, both of these branches make a large contribution to κ_{lat} as discussed before. Additionally, the calculated electronic thermal conductivity κ_e has a trend similar to that of σ , and the value of κ_e is much smaller than that of κ_{lat} as seen in Figure 5b.

Dimensionless Figure of Merit ZT . With all the transport properties available, the figures of merit, ZT s, for p- and n-type GeAs_2 as a function of carrier concentration at 300 and 800 K can be determined. The results are plotted in Figure 6a,b, respectively. The significant increase in ZT values at elevated temperature mainly stems from the decreased value of κ_{lat} . The electron doping is superior to hole doping due to a relatively large τ . A moderate peak value of ZT (0.46) in n-type GeAs_2 is obtained at 300 K. Because of ultralow intrinsic κ_{lat} and exceptionally high σ , the ZT value increases with temperature, and a satisfactory ZT value of 2.78 is achieved along the b -axis with electron doping concentration of $\sim 3 \times 10^{20} \text{ cm}^{-3}$ at 800 K. Therefore, the layered GeAs_2 has great potential for thermoelectric applications.

It is worth mentioning that the deformation potential theory adopted in our calculations is based on the scattering process between the electron and longitudinal acoustic phonon,⁶² which can provide a good prediction for ZT peaks at high temperature, because the acoustic phonon scattering is predominant in such conditions (like 800 K).^{63–65} However, it may lead to an overestimate of room-temperature ZT values, because the optical and acoustic phonon scattering contribute comparably at room temperature in some cases.⁶⁶

CONCLUSIONS

Using semiclassical Boltzmann transport theory, in combination with first-principles calculations, we have systematically studied the intrinsic thermoelectric properties of layered bulk GeAs_2 by focusing on its Seebeck coefficient, electrical conductivity, and thermal conductivity. Our results show that a large power factor

of 3.8 (4.2) mW/mK^2 can be achieved with electron doping along the out-of-plane direction at 300 (800) K due to the strong interlayer interaction, where quasicovalent bonding is formed by the unpaired electrons of As atoms. A low out-of-plane lattice thermal conductivity κ_b of 1.42 (0.53) W/mK is obtained at 300 K (800 K) because of strong anharmonicity between the adjacent layers. Due to the ultralow intrinsic lattice thermal conductivity and the exceptional large electrical conductivity, a maximum ZT value of 0.46 (2.78) is obtained with optimal electron doping at 300 (800) K. Our study suggests that the layered GeAs_2 is a promising material for thermoelectric applications, and may operate at intermediate temperatures. It will be worthwhile to study similar layered materials.

AUTHOR INFORMATION

Corresponding Author

*E-mail: qianwang2@pku.edu.cn.

ORCID

Qian Wang: 0000-0002-9766-4617

Puru Jena: 0000-0002-2316-859X

Notes

The authors declare no competing financial interest.

ACKNOWLEDGMENTS

This work is partially supported by grants from the National Natural Science Foundation of China (NSFC-51471004), and the National Key Research and Development Program of China (Grant 2016YFE0127300). P.J. acknowledges support by the U.S. Department of Energy, Office of Basic Energy Sciences, Division of Materials Sciences and Engineering, under Award #DE-FG02-96ER45579. The authors thank the crew of the Center for Computational Materials Science, the Institute for Materials Research, Tohoku University (Japan), for their continuous support of the HITACHI SR16000 supercomputing facility.

REFERENCES

- (1) Li, L.; Yu, Y.; Ye, G. J.; Ge, Q.; Ou, X.; Wu, H.; Feng, D.; Chen, X. H.; Zhang, Y. Black phosphorus field-effect transistors. *Nat. Nanotechnol.* **2014**, *9*, 372–377.
- (2) Lee, C.; Yan, H.; Brus, L. E.; Heinz, T. F.; Hone, J.; Ryu, S. Anomalous lattice vibrations of single- and few-layer MoS_2 . *ACS Nano* **2010**, *4*, 2695–2700.
- (3) Zhao, L.-D.; Lo, S.-H.; Zhang, Y.; Sun, H.; Tan, G.; Uher, C.; Wolverton, C.; Dravid, V. P.; Kanatzidis, M. G. Ultralow thermal

conductivity and high thermoelectric figure of merit in SnSe crystals. *Nature* **2014**, *508*, 373–377.

(4) Radisavljevic, B.; Radenovic, A.; Brivio, J.; Giacometti, i. V.; Kis, A. Single-layer MoS₂ transistors. *Nat. Nanotechnol.* **2011**, *6*, 147–150.

(5) Novoselov, K. S.; Geim, A. K.; Morozov, S. V.; Jiang, D.; Zhang, Y.; Dubonos, S. V.; Grigorieva, I. V.; Firsov, A. A. Electric field effect in atomically thin carbon films. *Science* **2004**, *306*, 666–669.

(6) Wang, X.; Kajiyama, S.; Iinuma, H.; Hosono, E.; Oro, S.; Moriguchi, I.; Okubo, M.; Yamada, A. Pseudocapacitance of MXene nanosheets for high-power sodium-ion hybrid capacitors. *Nat. Commun.* **2015**, *6*, 6544.

(7) Guo, Z.; Zhang, H.; Lu, S.; Wang, Z.; Tang, S.; Shao, J.; Sun, Z.; Xie, H.; Wang, H.; Yu, X. F.; Chu, P. K. From black phosphorus to phosphorene: basic solvent exfoliation, evolution of Raman scattering, and applications to ultrafast photonics. *Adv. Funct. Mater.* **2015**, *25*, 6996–7002.

(8) Qiao, J.; Kong, X.; Hu, Z.-X.; Yang, F.; Ji, W. High-mobility transport anisotropy and linear dichroism in few-layer black phosphorus. *Nat. Commun.* **2014**, *5*, 4475.

(9) Shulenburg, L.; Baczewski, A. D.; Zhu, Z.; Guan, J.; Tománek, D. The nature of the interlayer interaction in bulk and few-layer phosphorus. *Nano Lett.* **2015**, *15*, 8170–8175.

(10) Luo, X.; Lu, X.; Koon, G. K. W.; Castro Neto, A. H.; Özyilmaz, B.; Xiong, Q.; Quek, S. Y. Large frequency change with thickness in interlayer breathing mode-significant interlayer interactions in few layer black phosphorus. *Nano Lett.* **2015**, *15*, 3931–3938.

(11) Dong, S.; Zhang, A.; Liu, K.; Ji, J.; Ye, Y. G.; Luo, X. G.; Chen, X. H.; Ma, X.; Jie, Y.; Chen, C.; Wang, X.; Zhang, Q. Ultralow-frequency collective compression mode and strong interlayer coupling in multilayer black phosphorus. *Phys. Rev. Lett.* **2016**, *116*, 087401.

(12) Zhao, Y.; Qiao, J.; Yu, P.; Hu, Z.; Lin, Z.; Lau, S. P.; Liu, Z.; Ji, W.; Chai, Y. Extraordinarily strong interlayer interaction in 2D layered PtS₂. *Adv. Mater.* **2016**, *28*, 2399–2407.

(13) Zhao, Y.; Qiao, J.; Yu, Z.; Yu, P.; Xu, K.; Lau, S. P.; Zhou, W.; Liu, Z.; Wang, X.; Ji, W.; Chai, Y. High electron mobility and air stable 2D layered PtSe₂ FETs. *Adv. Mater.* **2017**, *29*, 1604230.

(14) Tongay, S.; Zhou, J.; Ataca, C.; Lo, K.; Matthews, T. S.; Li, J.; Grossman, J. C.; Wu, J. Thermally driven crossover from indirect toward direct bandgap in 2D semiconductors: MoSe₂ versus MoS₂. *Nano Lett.* **2012**, *12*, 5576–5580.

(15) Luo, X.; Zhao, Y.; Zhang, J.; Xiong, Q.; Quek, S. Y. Anomalous frequency trends in MoS₂ thin films attributed to surface effects. *Phys. Rev. B: Condens. Matter Mater. Phys.* **2013**, *88*, 075320.

(16) Kang, J.; Jariwala, D.; Ryder, C. R.; Wells, S. A.; Choi, Y.; Hwang, E.; Cho, J. H.; Marks, T. J.; Hersam, M. C. Probing out-of-plane charge transport in black phosphorus with graphene-contacted vertical field-effect transistors. *Nano Lett.* **2016**, *16*, 2580–2585.

(17) Sengupta, A.; Audiffred, M.; Heine, T.; Niehaus, T. A. Stacking dependence of carrier transport properties in multilayered black phosphorus. *J. Phys.: Condens. Matter* **2016**, *28*, 075001.

(18) Alsaleh, N. M.; Singh, N.; Schwingenschlög, U. Role of interlayer coupling for the power factor of CuSbS₂ and CuSbSe₂. *Phys. Rev. B: Condens. Matter Mater. Phys.* **2016**, *94*, 125440.

(19) Du, Y.; Maassen, J.; Wu, W.; Luo, Z.; Xu, X.; Ye, P. D. Auxetic black phosphorus: A 2D material with negative poisson's ratio. *Nano Lett.* **2016**, *16*, 6701–6708.

(20) Appalakondaiah, S.; Vaitheeswaran, G.; Lebègue, S.; Christensen, N. E.; Svane, A. Effect of van der Waals interactions on the structural and elastic properties of black phosphorus. *Phys. Rev. B: Condens. Matter Mater. Phys.* **2012**, *86*, 035105.

(21) Gorai, P.; Toberer, E. S.; Stevanovic, V. Computational identification of promising thermoelectric materials among known quasi-2D binary compounds. *J. Mater. Chem. A* **2016**, *4*, 11110–11116.

(22) Perdew, J. P.; Burke, K.; Ernzerhof, M. Generalized gradient approximation made simple. *Phys. Rev. Lett.* **1996**, *77*, 3865.

(23) Kresse, G.; Furthmüller, J. Efficient iterative schemes for ab initio total-energy calculations using a plane-wave basis set. *Phys. Rev. B: Condens. Matter Mater. Phys.* **1996**, *54*, 11169.

(24) Grimme, S. Semiempirical GGA-type density functional constructed with a long-range dispersion correction. *J. Comput. Chem.* **2006**, *27*, 1787–1799.

(25) Grimme, S.; Antony, J.; Ehrlich, S.; Krieg, H. A consistent and accurate ab initio parametrization of density functional dispersion correction (DFT-D) for the 94 elements H-Pu. *J. Chem. Phys.* **2010**, *132*, 154104.

(26) Cutler, M.; Leavy, J. F.; Fitzpatrick, R. L. Electronic transport in semimetallic cerium sulfide. *Phys. Rev.* **1964**, *133*, A1143–A1152.

(27) Snyder, G. J.; Toberer, E. S. Complex thermoelectric materials. *Nat. Mater.* **2008**, *7*, 105–114.

(28) Tran, F.; Blaha, P. Accurate band gaps of semiconductors and insulators with a semilocal exchange-correlation potential. *Phys. Rev. Lett.* **2009**, *102*, 226401.

(29) Boulet, P.; Record, M.-C. Influence of the modified Becke-Johnson exchange potential on thermoelectric properties: Application to Mg₂Si. *J. Chem. Phys.* **2011**, *135*, 234702.

(30) Ong, K. P.; Singh, D. J.; Wu, P. Analysis of the thermoelectric properties of n-type ZnO. *Phys. Rev. B: Condens. Matter Mater. Phys.* **2011**, *83*, 115110.

(31) Lv, H. Y.; Lu, W. J.; Shao, D. F.; Sun, Y. P. Enhanced thermoelectric performance of phosphorene by strain-induced band convergence. *Phys. Rev. B: Condens. Matter Mater. Phys.* **2014**, *90*, 085433.

(32) Li, W.; Carrete, J.; Katcho, N. A.; Mingo, N. ShengBTE: A solver of the Boltzmann transport equation for phonons. *Comput. Phys. Commun.* **2014**, *185*, 1747–1758.

(33) Omini, M.; Sparavigna, A. An iterative approach to the phonon Boltzmann equation in the theory of thermal conductivity. *Phys. B* **1995**, *212*, 101–112.

(34) Toberer, E. S.; Baranowski, L. L.; Dames, C. Advances in thermal conductivity. *Annu. Rev. Mater. Res.* **2012**, *42*, 179–209.

(35) Kim, H.-S.; Gibbs, Z. M.; Tang, Y.; Wang, H.; Snyder, G. J. Characterization of Lorenz number with Seebeck coefficient measurement. *APL Mater.* **2015**, *3*, 041506.

(36) Bryden, J. The crystal structures of the germanium-arsenic compounds: I. Germanium diarsenide, GeAs₂. *Acta Crystallogr.* **1962**, *15*, 167–171.

(37) Wu, P.; Huang, M. Stability, bonding, and electronic properties of silicon and germanium arsenides. *Phys. Status Solidi B* **2016**, *253*, 862–867.

(38) Rau, J. W.; Kannewurf, C. Optical absorption, reflectivity, and electrical conductivity in GeAs and GeAs₂. *Phys. Rev. B* **1971**, *3*, 2581.

(39) Zhao, L.; Wu, H.; Hao, S.; Wu, C.-I.; Zhou, X.; Biswas, K.; He, J.; Hogan, T. P.; Uher, C.; Wolverton, C.; et al. All-scale hierarchical thermoelectrics: MgTe in PbTe facilitates valence band convergence and suppresses bipolar thermal transport for high performance. *Energy Environ. Sci.* **2013**, *6*, 3346–3355.

(40) Zhao, L.-D.; Chang, C.; Tan, G.; Kanatzidis, M. G. SnSe: a remarkable new thermoelectric material. *Energy Environ. Sci.* **2016**, *9*, 3044–3060.

(41) Zhao, L.-D.; Tan, G.; Hao, S.; He, J.; Pei, Y.; Chi, H.; Wang, H.; Gong, S.; Xu, H.; Dravid, V. P.; et al. Ultrahigh power factor and thermoelectric performance in hole-doped single-crystal SnSe. *Science* **2016**, *351*, 141–144.

(42) Guo, R.; Wang, X.; Kuang, Y.; Huang, B. First-principles study of anisotropic thermoelectric transport properties of IV-VI semiconductor compounds SnSe and SnS. *Phys. Rev. B: Condens. Matter Mater. Phys.* **2015**, *92*, 115202.

(43) Kuroki, K.; Arita, R. "Pudding mold" band drives large thermopower in Na_xCoO₂. *J. Phys. Soc. Jpn.* **2007**, *76*, 083707.

(44) Wang, F. Q.; Zhang, S.; Yu, J.; Wang, Q. Thermoelectric properties of single-layered SnSe sheet. *Nanoscale* **2015**, *7*, 15962–15970.

(45) Hao, S.; Shi, F.; Dravid, V. P.; Kanatzidis, M. G.; Wolverton, C. Computational prediction of high thermoelectric performance in hole doped layered GeSe. *Chem. Mater.* **2016**, *28*, 3218–3226.

(46) Kutorasinski, K.; Wiendlocha, B.; Kaprzyk, S.; Tobola, J. Electronic structure and thermoelectric properties of n- and p-type

SnSe from first-principles calculations. *Phys. Rev. B: Condens. Matter Mater. Phys.* **2015**, *91*, 205201.

(47) Madsen, G. K. H.; Singh, D. J. BoltzTraP. A code for calculating band-structure dependent quantities. *Comput. Phys. Commun.* **2006**, *175*, 67–71.

(48) Kumar, S.; Schwingenschlögl, U. Thermoelectric performance of functionalized Sc 2 C MXenes. *Phys. Rev. B: Condens. Matter Mater. Phys.* **2016**, *94*, 035405.

(49) Gandi, A. N.; Alshareef, H. N.; Schwingenschlögl, U. Thermoelectric performance of the MXenes M₂CO₂ (M= Ti, Zr, or Hf). *Chem. Mater.* **2016**, *28*, 1647–1652.

(50) Madsen, G. K. H. Automated search for new thermoelectric materials: The case of LiZnSb. *J. Am. Chem. Soc.* **2006**, *128*, 12140–12146.

(51) He, J.; Amsler, M.; Xia, Y.; Naghavi, S. S.; Hegde, V. I.; Hao, S.; Goedecker, S.; Ozoliņš, V.; Wolverton, C. Ultralow thermal conductivity in full heusler semiconductors. *Phys. Rev. Lett.* **2016**, *117*, 046602.

(52) May, A. F.; Toberer, E. S.; Saramat, A.; Snyder, G. J. Characterization and analysis of thermoelectric transport in n-type Ba₈Ga_{16-x}Ge_{30+x}. *Phys. Rev. B: Condens. Matter Mater. Phys.* **2009**, *80*, 125205.

(53) Bilc, D. I.; Hautier, G.; Waroquiers, D.; Rignanese, G.-M.; Ghosez, P. Low-dimensional transport and large thermoelectric power factors in bulk semiconductors by band engineering of highly directional electronic states. *Phys. Rev. Lett.* **2015**, *114*, 136601.

(54) Popescu, A.; Woods, L.; Martin, J.; Nolas, G. Model of transport properties of thermoelectric nanocomposite materials. *Phys. Rev. B: Condens. Matter Mater. Phys.* **2009**, *79*, 205302.

(55) Bardeen, J.; Shockley, W. Deformation potentials and mobilities in non-polar crystals. *Phys. Rev.* **1950**, *80*, 72.

(56) Zhao, T.; Shi, W.; Xi, J.; Wang, D.; Shuai, Z. Intrinsic and extrinsic charge transport in CH₃NH₃PbI₃ perovskites predicted from first-principles. *Sci. Rep.* **2016**, *7*, 19968.

(57) Xi, J.; Long, M.; Tang, L.; Wang, D.; Shuai, Z. First-principles prediction of charge mobility in carbon and organic nanomaterials. *Nanoscale* **2012**, *4*, 4348–4369.

(58) Björkman, T. van der Waals density functional for solids. *Phys. Rev. B: Condens. Matter Mater. Phys.* **2012**, *86*, 165109.

(59) Hu, X.; Jood, P.; Ohta, M.; Kunii, M.; Nagase, K.; Nishiate, H.; Kanatzidis, M. G.; Yamamoto, A. Power generation from nano-structured PbTe-based thermoelectrics: comprehensive development from materials to modules. *Energy Environ. Sci.* **2016**, *9*, 517–529.

(60) Zhu, L.; Zhang, G.; Li, B. Coexistence of size-dependent and size-independent thermal conductivities in phosphorene. *Phys. Rev. B: Condens. Matter Mater. Phys.* **2014**, *90*, 214302.

(61) Wang, F. Q.; Yu, J.; Wang, Q.; Kawazoe, Y.; Jena, P. Lattice thermal conductivity of penta-graphene. *Carbon* **2016**, *105*, 424–429.

(62) Bardeen, J.; Shockley, W. Deformation potentials and mobilities in non-polar crystals. *Phys. Rev.* **1950**, *80*, 72–80.

(63) Wang, H.; Pei, Y.; LaLonde, A. D.; Snyder, G. J. Weak electron-phonon coupling contributing to high thermoelectric performance in n-type PbSe. *Proc. Natl. Acad. Sci. U. S. A.* **2012**, *109*, 9705–9709.

(64) Pei, Y.; Shi, X.; LaLonde, A.; Wang, H.; Chen, L.; Snyder, G. J. Convergence of electronic bands for high performance bulk thermoelectrics. *Nature* **2011**, *473*, 66.

(65) Pei, Y.; Gibbs, Z. M.; Gloskovskii, A.; Balke, B.; Zeier, W. G.; Snyder, G. J. Optimum carrier concentration in n-type PbTe thermoelectrics. *Adv. Energy Mater.* **2014**, *4*, 1400486.

(66) Zhao, T.; Sun, Y.; Shuai, Z.; Wang, D. GeAs₂: A IV–V group two-dimensional semiconductor with ultralow thermal conductivity and high thermoelectric efficiency. *Chem. Mater.* **2017**, *29*, 6261–6268.